Click Here for Full Article

Aerosol optical properties and radiative effects in the Yangtze Delta region of China

Xiangao Xia,[1] Zhanqing Li,[1,2] Brent Holben,[3] Pucai Wang,[1] Tom Eck,[3] Hongbin Chen,[1] Maureen Cribb,[2] and Yanxia Zhao[4]

[1] One year's worth of aerosol and surface irradiance data from September 2005 to August 2006 were obtained at Taihu, the second supersite for the East Asian Study of Tropospheric Aerosols: An International Regional Experiment (EAST-AIRE). Aerosol optical properties derived from measurements by a Sun photometer were analyzed. The aerosol data were used together with surface irradiance data to quantitatively estimate aerosol effects on surface shortwave radiation (SWR) and photosynthetically active radiation (PAR). The annual mean aerosol optical depth at 500 nm is 0.77, and mean Ångstrom wavelength exponent is 1.17. The annual mean aerosol single scattering albedo and mean aerosol asymmetry factor at 440 nm are 0.90 and 0.72, respectively. Both parameters show a weak seasonal variation, with small values occurring during the winter and larger values during the summer. Clear positive relationships between relative humidity and aerosol properties suggest aerosol hygroscopic growth greatly modifies aerosol properties. The annual mean aerosol direct radiative forcing at the surface (ADRF) is -38.4 W m^{-2} and -17.8 W m^{-2} for SWR and PAR, respectively. Because of moderate absorption, the instantaneous ADRF at the top of the atmosphere derived from CERES SSF data is close to zero. Heavy aerosol loading in this region leads to -112.6 W m^{-2} and -45.5 W m^{-2} reduction in direct and global SWR, but 67.1 W m^{-2} more diffuse SWR reaching the surface. With regard to PAR, the annual mean differences in global, direct and diffuse irradiance are -23.1 W m^{-2}, -65.2 W m^{-2} and 42.1 W m^{-2} with and without the presence of aerosol, respectively.

1. Introduction

[2] The rapid economic development and population expansion since the mid-1970s has led to heavy aerosol loading over much of China [*Luo et al.*, 2001; *Qiu and Yan*, 2000; *Xia et al.*, 2007a; *Zong et al.*, 2005]. Studies indicate links between fine particulate matter and numerous health problems because these particles are so small that they are able to penetrate the deepest parts of the lungs [*Ren et al.*, 1999]. It is believed that aerosols influence plant growth and carbon cycling through their effects on the surface energy budget [*Chameides et al.*, 1999]. Studies have established that aerosols are closely related to some impor-tant environment issues such as acid rain and tropospheric ozone pollution [*Wang*, 1999]. Aerosols influence both visibility and climate through the scattering and absorption of solar radiation [*Ramanathan et al.*, 2001; *Wang et al.*, 2001]. A combination of heavy aerosol loading and strong absorption of aerosols is believed to have played an impor-tant role in the regional temperature and precipitation pattern changes since the mid-1970s in China via aerosol direct and indirect effects [*Li et al.*, 1995; *Xu*, 2001; *Menon et al.*, 2002].

[3] With regard to the direct effect of aerosols on the surface energy budget under clear-sky conditions, key optical parameters that need estimation include the aerosol optical depth (AOD), the aerosol single scattering albedo (SSA) (the ratio of scattering coefficient to extinction coefficient) and the aerosol asymmetry factor (ASY). A few simultaneous measurements of aerosol optical proper-ties and surface irradiance have been made in northern China, which are used to estimate aerosol direct effects at the surface and at the top of the atmosphere [*Cheng et al.*, 2006; *Li et al.*, 2007a; *Xia et al.*, 2007b]. Aerosol effects on surface irradiance in eastern China were examined on the basis of measurements and model simulations [*Xu et al.*, 2003]. Note that observations of aerosol properties and

[1]Laboratory for Middle Atmosphere and Global Environment Observa-tion, Institute of Atmospheric Physics, Chinese Academy of Sciences, Beijing, China.
[2]Department of Atmospheric and Oceanic Science, University of Maryland, College Park, Maryland, USA.
[3]Laboratory for Atmospheres, NASA Goddard Space Flight Center, Greenbelt, Maryland, USA.
[4]Chinese Academy of Meteorological Sciences, Chinese Meteorological Administration, Beijing, China.

aerosol radiative effects are still urgently required because there is quite a large spatial and temporal variation of complex aerosols throughout the vast territory of China [*Li*, 2004; *Mao and Li*, 2005; *Wang et al.*, 2001].

[4] A project titled the "East Asian Study of Tropospheric Aerosols: An International Regional Experiment (EAST-AIRE)" commenced in 2004 [*Li et al.*, 2007b]. A major goal of the project is to assess aerosol effects on the energy balance through the establishment of some baseline aerosol and radiation observation sites in China. These baseline stations are equipped with a large number of instruments that are operated following rigorous procedures to comply with the requirements of the BSRN [*Ohmura et al.*, 1998] and AERONET [*Holben et al.*, 1998]. The first site was established at Xianghe in northern China and the data were used to study the influence of aerosols on the energy balance [*Li et al.*, 2007a; *Xia et al.*, 2007b]. The Taihu site, the second supersite located in the Yangtze delta region, was established in September 2005 and continuous measurements have been taken since its commencement. The data are used here to investigate aerosol effects on irradiance at the surface and at the top of the atmosphere in this region where anthropogenic activities lead to high aerosol loading [*Mao and Li*, 2005; *Song and Lu*, 2006].

2. Site Description and Instrumentation

[5] The Taihu observatory was established right at the edge of the Taihu lake (31.702°N, 120.358°E, 10 m above sea level) surrounded by big cities in the Yangtze delta region, namely, Shanghai to the east, Nanjing to the west, and Hanzhou to the north. The region is a key industrial and agricultural area that experiences high aerosol loadings, which is clearly shown by the annual mean Moderate Resolution Imaging Spectroradiometer (MODIS) AOD (collection 5) [*Li et al.*, 2007c]. The MODIS aerosol collection 5 data in China were evaluated using ground-based remote sensing data [*Mi et al.*, 2007; *Li et al.*, 2007c]. A CIMEL Sun/sky radiometer and a set of broadband radiometers were installed side by side. A Total Sky Imager (TSI) was employed to take snapshots of the overhead sky every minute during the daytime. One year's worth of data, from September 2005 to August 2006, is analyzed in this study.

2.1. AERONET Data

[6] A CIMEL Sun/sky radiometer was installed in September 2005 and Taihu has joined the Aerosol Robotic Network (AERONET) since then [*Holben et al.*, 1998]. AOD at 340, 380, 440, 500, 675, 870, 1020, and 1640 nm with an uncertainty of 0.01~0.02 can be derived from direct radiance measurements [*Eck et al.*, 1999]. The measurements at 940 nm are used for the derivation of the water vapor column amount. The aerosol size distribution, refractive index and single scattering albedo are retrieved from the sky radiance measurements and AODs at 440, 675, 870, and 1020 nm [*Dubovik et al.*, 2000, 2006]. Data employed are the level 2.0 quality-assured data that have been prefield and postfield calibrated, automatically cloud-screened and manually inspected (http://aeronet.gsfc.nasa.gov) from the

latest release of the Version 2 AERONET data. The Version 2 almucantar retrievals of aerosol parameters for aerosol optical depth at 440 nm larger than 0.4 have been used in the study.

2.2. Broadband Surface Solar Radiation Data

[7] Surface irradiances are measured by a set of solar radiometers. The sample resolution is 1 Hz but 1-min means and standard deviations are saved to a Campbell data logger. Global shortwave radiation (SWR) are measured directly by Kipp-Zonen CM21 and CM11 radiometers and indirectly by an Eppley Normal Incidence Pyrheliometer (NIP) and a black-and-white radiometer (B&W), both mounted on an EKO STR-22 solar tracker to measure solar direct and diffuse radiation, respectively. A redundant set of broadband radiometers was used to ensure the precision of measurements and to monitor anomalous measurements due to physical problems (e.g., misaligned solar shadowing disk, sensor dome contamination, etc.). A Kipp-Zonen PAR-LITE quantum sensor is used to measure photon number density in the visible spectrum (400–700 nm). The data are quality checked using Baseline Surface Radiation Network (BSRN) quality control procedures [*Ohmura et al.*, 1998]. The data quality and consistency are guaranteed by daily instrument maintenance and checking. Because of the nonideal angular response and well known zero offset of the CM21 and CM11 radiometers, global SWR data used in this paper were calculated by summing the direct beam radiation (multiplied by cosine of the solar zenith angle) and the diffuse horizontal radiation [*Michalsky et al.*, 1999; *Dutton et al.*, 2001]. The field measurement uncertainties were estimated to be 3%, 6%, and 6% for direct, diffuse and global measurements using NIP and B&W radiometers [*Stoffel*, 2005].

2.3. Total Sky Imager (TSI) Data

[8] A TSI-440 was installed to take pictures of the overhead sky every minute during the daytime. The TSI-440 model is a full-color sky camera with a software package that operates the instrument and performs some data processing functions. The cloud fraction is derived from the snapshots.

2.4. Top of the Atmosphere (TOA) CERES Data

[9] In addition to ground-based measurements, this study also employs satellite measurements of SWR reflected at the top of the atmosphere (TOA) obtained from the Clouds and the Earth's Radiant Energy System (CERES). The CERES instrument, deployed on the Earth Observing System's Terra and Aqua satellite platforms, consists of a scanning radiometer collecting radiometric measurements in three channels, i.e., 0.3–5 μm, 8–12 μm and 0.3–100 μm [*Wielicki et al.*, 1996]. One set of products from the CERES instruments is the Single Satellite Footprint (SSF) collection of hourly products. The SSF data are an integration of the coarser resolution CERES measurements (about 20 km at nadir) and data from higher-resolution imagers such as MODIS on the Terra and Aqua platforms. In general, two measurements were available for each day, one in the morning from the Terra platform and another in the early afternoon from the Aqua platform. Data from September to December 2005 are

Table 1. Seasonal Means and Standard Deviations of Aerosol Optical Depth at Five Wavelengths, i.e., 440 nm, 500 nm, 675 nm, 870 nm and 1020 nm, the Ångström Wavelength Exponent and Precipitable Water Vapor

	AOD_{1020}	AOD_{870}	AOD_{675}	AOD_{500}	AOD_{440}	$AWE_{440-870}$	PWV, cm
MAM	0.43 ± 0.19	0.49 ± 0.22	0.62 ± 0.28	0.81 ± 0.38	0.91 ± 0.43	0.90 ± 0.29	1.33 ± 0.60
JJA	0.33 ± 0.27	0.43 ± 0.35	0.61 ± 0.51	0.90 ± 0.73	1.02 ± 0.80	1.35 ± 0.19	4.16 ± 1.05
SON	0.31 ± 0.18	0.41 ± 0.24	0.59 ± 0.35	0.87 ± 0.51	0.99 ± 0.56	1.33 ± 0.18	2.17 ± 1.22
DJF	0.27 ± 0.14	0.32 ± 0.16	0.43 ± 0.21	0.60 ± 0.29	0.68 ± 0.32	1.11 ± 0.23	0.69 ± 0.46

employed in this study, as the CERES data are not yet available for 2006.

3. Clear-Sky Discrimination Using Broadband Radiation Data

[10] The focus here is the aerosol effects under clear-sky conditions, so the first step is to discriminate between cloudy and cloudless conditions. This is achieved using an empirical clear-sky detection algorithm proposed by *Long and Ackerman* [2000], with some modifications to better cope with the specific conditions under study. The method is briefly introduced here for completeness. First, a power law function of the cosine of the solar zenith angle is used to search for potential SWR measurements under cloudless conditions each day. Second, CM21 observations are normalized by the power law equation and a running standard deviation over successive 30-min periods is calculated to check temporal variability. The observation is deemed affected by cloud if the standard deviation is greater than 0.02. Third, the radiation data are excluded in the analysis if diffuse radiation is greater than the maximum diffuse radiation, i.e., $350 \times \mu^{0.5}$, where μ is the cosine of solar zenith angle. Finally, data are eliminated if the standard deviation of CM21 or B&W measurements within each minute is larger than 0.02. The data are accepted as observations made under cloud-free skies if they pass all the tests. The clear-sky radiation data are finally collocated with AERONET aerosol data to examine aerosol effects on surface irradiance.

4. Results

[11] Seasonal averages of aerosol optical properties derived from the CIMEL Sun photometer are first presented. A couple of parameterization equations are then developed to describe the relationships between AOD and surface irradiances, which are used to study aerosol radiative effects at the surface. Finally, instantaneous aerosol effect on energy budget at the TOA is derived from a combination of CERES-SSF and aerosol data.

### 4.1. Seasonal Variation of Aerosol Optical Properties

[12] Table 1 presents seasonal mean AODs at five wavelengths (i.e., 440, 500, 675, 870 and 1020 nm), Ångstrom wavelength exponents (AWE) and precipitable water vapor (PWV) in the unit of cm. The AWE is computed as the slope of the linear regression between ln(AOD) and ln(λ) at 440, 675, and 870 nm, where λ represents wavelength. The annual mean AOD at 500 nm is 0.77, being more than seven times that the minimum value (~0.10). The mean AOD here is relatively greater than observations in other suburban regions of China, such as 0.61 at Linan [*Xu et al.*, 2002], 0.56 at Miyun and 0.60 at Xinfeng [*Zhang et al.*,

2002] and 0.63 at Liaozhong [*Xia et al.*, 2007c]. It is equal to the mean AOD at Xianghe (0.77) [*Li et al.*, 2007a]. Heavy aerosol loading prevails all year round and the seasonal mean AODs at 500 nm are 0.81, 0.90, 0.87 and 0.60 in spring (MAM), in summer (JJA), in autumn (SON) and in winter (DJF), respectively. Three quarters of AODs are larger than 0.48 and one quarter of AODs are even larger than 1.0 (Figure 1a showing the histogram of AOD). Note that only one daily mean AOD from a total of 135 daily means at this site is less than 0.15, however, about 22% of the AODs at Xianghe are less than 0.15. The frequent cold air outbreaks can blow aerosols away in northern China, leading to a relatively greater occurrence of the background level of aerosol loading [*Xia et al.*, 2005]. However, the situation is quite different in this region where cold air outbreaks are relatively weaker than in northern China. The annual mean AWE is 1.17 and the seasonal mean AWEs are 0.90, 1.35, 1.33 and 1.11, respectively. A few cases with AWE less than 0.6 occurred in spring when dust events occasionally impacted the site. Three quarters of the AWEs are greater than 1.0 (Figure 1b). The large range of the AWE, from 0.3 to 1.8, suggests that there were different types of aerosols present (from very fine mode pollution to large coarse mode dust). The relationship between AWE and the aerosol fine fraction of extinction at four wavelengths are derived from available almucantar retrievals, which suggests that fine mode aerosols contribute to more than 75% of extinction at 440 nm and half extinction at 675 nm when AWE is larger than 1.0 (Figure 2).

[13] Table 2 presents seasonal averages of the real part (RE) and imaginary part (IM) of aerosol refractive index, the SSA, as well as the ASY at four wavelengths. The annual mean RE and IM at 440 nm are 1.43 and 0.012, respectively. The values of RE and IM at other three wavelengths are close to 1.48 and 0.008, respectively. There is a weak seasonal variation in the RE and IM, with small values occurring during the summer and larger values during the winter. The annual mean SSA at 440 nm is about 0.90 and the largest seasonal SSA approaches 0.93 that occurred in summer. The monthly SSA in November is about 0.91, which is less than the in situ measurements at the Linan site in November where the mean SSA of dry and ambient aerosols is about 0.93 and 0.95, respectively [*Xu et al.*, 2003]. The annual mean SSAs at four wavelengths are 0.90, 0.92, 0.92 and 0.91, respectively. The values are moderately larger than that in northern China, for example, in Beijing and Xianghe [*Li et al.*, 2007a; *Qiu et al.*, 2004; *Xia et al.*, 2006]. They are also slightly larger at 440 nm than those reported for Mexico City and the Maldives [*Dubovik et al.*, 2002] but for longer wavelengths they are much higher. The large range of the SSA, from 0.81 to 0.98, also suggests that there were quite different types of aerosols present (from
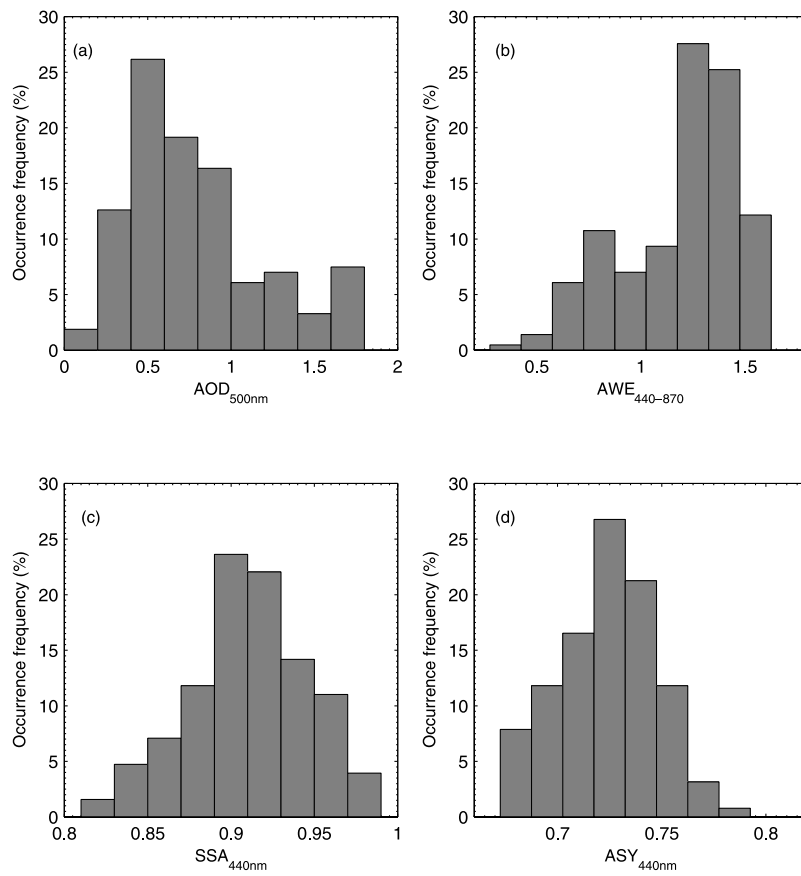
Figure 1. Histograms of (a) aerosol optical depth at 500 nm, (b) Ångström wavelength exponent, (c) single scattering albedo at 440 nm and (d) asymmetry factor at 440 nm.
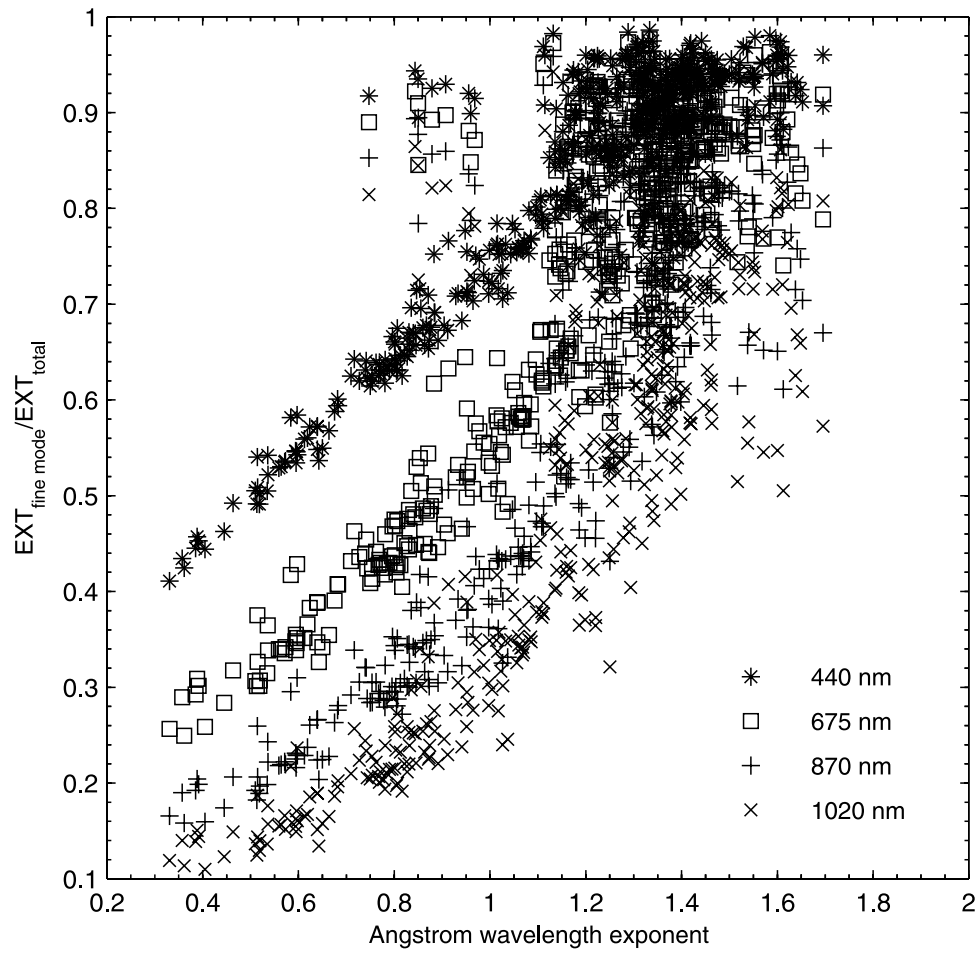
Figure 2. Ångström wavelength exponent versus the ratio of fine mode extinction to total extinction at 440 nm, 675 nm, 870 nm and 1020 nm.

Table 2. Seasonal Means and Standard Deviations of Single Scattering Albedo, Real Part and Imaginary Part of Refractive Index as Well as Asymmetry Factor at Four Wavelengths, i.e., 440 nm, 675 nm, 870 nm and 1020 nm[a]

	Wavelength			
	440 nm	675 nm	870 nm	1020 nm
	RE			
MAM	1.451 ± 0.062	1.495 ± 0.048	1.508 ± 0.039	1.504 ± 0.035
JJA	1.406 ± 0.046	1.429 ± 0.049	1.440 ± 0.051	1.435 ± 0.053
SON	1.428 ± 0.056	1.454 ± 0.049	1.468 ± 0.048	1.467 ± 0.047
DJF	1.449 ± 0.058	1.485 ± 0.053	1.502 ± 0.052	1.508 ± 0.052
	IM			
MAM	0.009 ± 0.004	0.005 ± 0.003	0.005 ± 0.003	0.004 ± 0.003
JJA	0.007 ± 0.002	0.006 ± 0.002	0.005 ± 0.003	0.005 ± 0.003
SON	0.011 ± 0.005	0.008 ± 0.004	0.008 ± 0.004	0.008 ± 0.004
DJF	0.019 ± 0.006	0.011 ± 0.004	0.012 ± 0.005	0.012 ± 0.005
	SSA			
MAM	0.896 ± 0.022	0.934 ± 0.021	0.939 ± 0.027	0.942 ± 0.030
JJA	0.936 ± 0.034	0.939 ± 0.034	0.936 ± 0.039	0.931 ± 0.044
SON	0.915 ± 0.031	0.926 ± 0.026	0.920 ± 0.031	0.913 ± 0.035
DJF	0.865 ± 0.037	0.891 ± 0.035	0.879 ± 0.040	0.869 ± 0.045
	ASY			
MAM	0.719 ± 0.019	0.664 ± 0.022	0.656 ± 0.030	0.663 ± 0.035
JJA	0.733 ± 0.027	0.664 ± 0.033	0.630 ± 0.028	0.617 ± 0.028
SON	0.725 ± 0.021	0.648 ± 0.031	0.612 ± 0.034	0.599 ± 0.034
DJF	0.711 ± 0.024	0.636 ± 0.030	0.612 ± 0.031	0.607 ± 0.033

[a]Note that retrievals for aerosol optical depth at 440 nm less than 0.4 have been screened out in the calculation.

strong absorbing aerosols to nearly pure scattering aerosols). One quarter of the SSA is less than 0.90 and one quarter of the SSA is larger than 0.93 (Figure 1c). There is also a weak seasonal trend in the SSA, with large values occurring during the summer and smaller values during the winter. The annual mean ASYs gradually decreases from 0.72 at 440 nm to 0.62 at 1020 nm. The values of ASY during the autumn and the winter are generally less than those during the spring and the summer. The ASY at 440 nm ranges from 0.66 to 0.80 and half of ASYs are within 0.71 to 0.74 (Figure 1d). The ASYs here is larger than those in northern China. This is partly because the fine mode radius here is larger than that in northern China. For example, the fine mode volume median radius at the Taihu site averages 0.181 μm over a range of AOD from 0.6 to 1.0, while it is 0.168 μm in northern China.

[14] Figure 3 presents the mean SSAs (Figure 3a), RE (Figure 3b) and IM (Figure 3c) and ASY (Figure 3d) in each of seven AOD (500 nm) bins, which are averages of retrievals made from more than ten individual almucantar scans. SSA at 440 nm is generally less than that at 675 nm. This is possibly due to the influence of organic carbon that accounts for ~50% of the $PM_{2.5}$ mass in this region [*Xu et al.*, 2002]. Both SSA and ASY increase with AOD. The magnitude of changes in the SSA is significant, with a range of 0.05−0.07 over a range of AOD from 0.3 to 1.9. The ASY varies from 0.04 to 0.08 over the same AOD range. This is partly because the fine mode particle size increases with AOD, which is clearly seen in Figure 4 (showing the size distribution in each of the seven AOD bins). These trends in particle size are observed in other regions and so dynamic changes of aerosol optical properties with aerosol loading are modeled on the basis of this

trend [*Eck et al.*, 2005]. The fine mode radius, the SSA and the ASY show clear positive dependence on AOD. This may result from the mixed influence of the hygroscopic growth, coagulation growth and variable species of aerosol emissions from various sources, such as coarse mode airborne dust versus fine mode anthropogenic pollution [*Li et al.*, 2007a]. For a fixed aerosol composition, the hygroscopic growth under humid environment should lead to the increase in fine mode radius, enhance scattering (thus increasing the AOD), weaken the aerosol absorption efficiency (thus increasing the SSA), and enlarge the particle size (thus increasing the ASY). This is confirmed by Figure 5, in which we can see positive relations between relative humidity (measured at the surface at a nearby meteorological station) and AOD (Figure 5, top left), the SSA (Figure 5, top right) and the ASY (Figure 5, bottom left). This suggests that aerosol properties are greatly modified by condensed water. As a matter of fact, it has been indicated that condensed water typically contributes ~40% to the light scattering budget in this region [*Xu et al.*, 2002].

## 4.2. Comparison Between Measurements and Simulations of Surface Irradiance

[15] Surface irradiances are calculated using the Santa Barbara DISORT Atmospheric Radiative Transfer model (SBDART) [*Ricchiazzi et al.*, 1998]. The ozone, water vapor and surface albedo data driving the model are from the Total Ozone Mapping Spectrometer (TOMS) (http://toms.gsfc.nasa.gov), AERONET and MODIS retrievals [*Schaaf et al.*, 2002], respectively. The aerosol inputs to the SBDART are the AOD, SSA and ASY at four AERONET wavelengths, i.e., 440, 675, 870 and 1020 nm, which are used to interpolate and extrapolate into the spectral divisions of SBDART. SBDART relies on the LOWTRAN-7 atmospheric transmission data and the radiative transfer equation is numerically integrated with the DISORT radiative transfer module with four radiation streams. The SBDART agreed to better than 3% in the broadband calculations of irradiance with measurements [*Halthore et al.*, 2005]. A comparison between the measured and modeled instantaneous surface irradiances is shown in Figure 6, showing excellent agreements. The mean bias errors (MBE: mean observation minus mean simulation) are 1.2 W m^{-2}, −1.2 W m^{-2}, 6.8 W m^{-2} and 6.9 W m^{-2} for direct, diffuse, global SWR and global PAR, respectively. The MBE values are much less than root mean square errors (RMSE) and are well within model and measurement uncertainties. Note that photo number density is converted to energy through multiplying the individual ratio of radiative energy to photon number density, which is derived from the SBDART simulations. Accordingly, PAR presented hereafter has units of W m^{-2} rather than μmol m^{-2} s^{-1}.

4.3. Instantaneous and Diurnal Aerosol Direct Radiative Forcing

[16] Aerosol direct radiative forcing (ADRF) refers to the difference in surface irradiance with and without the presence of aerosols. The first term can be directly observed by ground-based or spaceborne radiometers. The second term cannot be observed directly. Two methods are usually used to derive this quantity: (1) calculation from a radiative
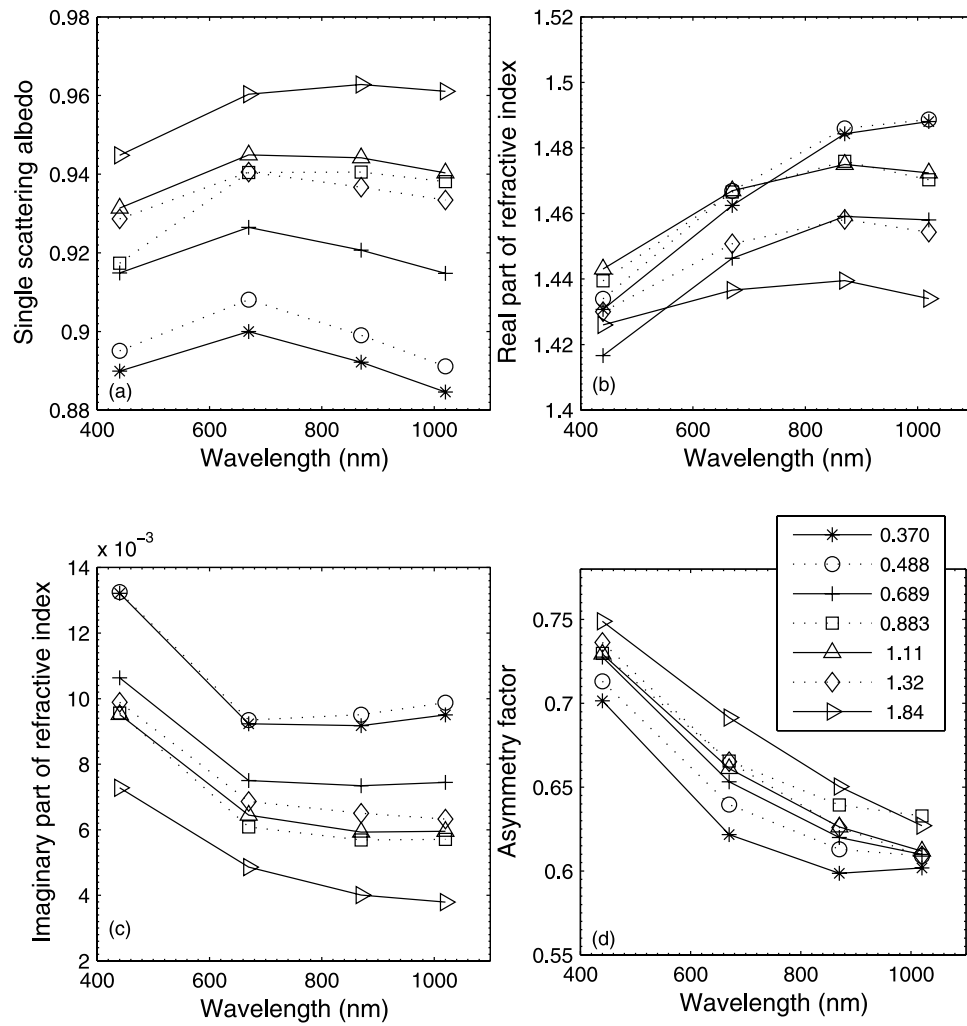
Figure 3. (a) Averaged aerosol single scattering albedo, (b) real part of refractive index, (c) imaginary part of refractive index and (d) asymmetry factor in each of the seven bins of aerosol optical depth at 500 nm, which is calculated if more than 10 almucantar scans are available.
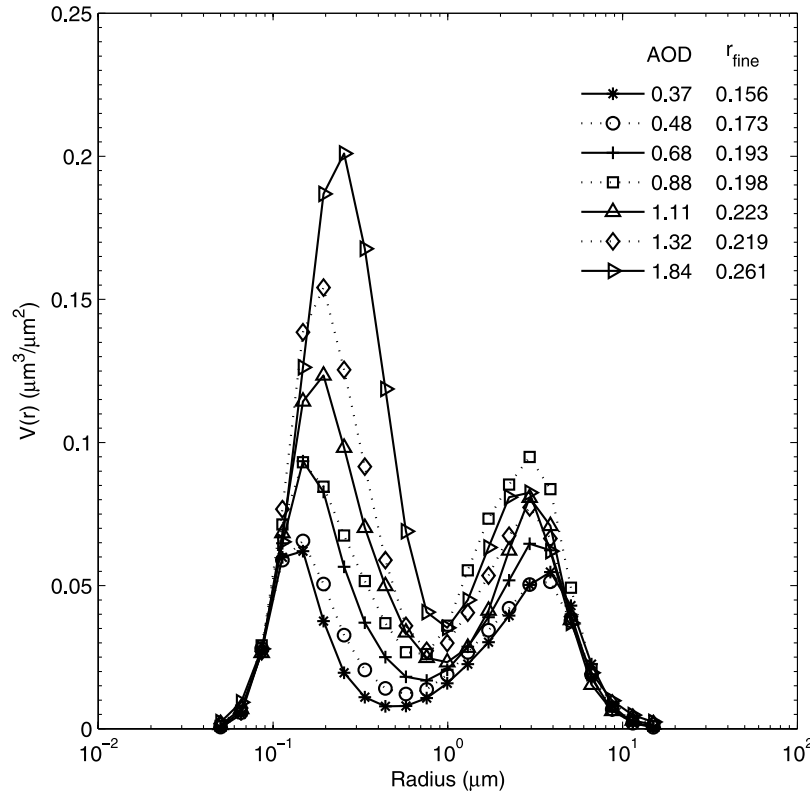
Figure 4. Same as Figure 3 but for the volume size distribution, dV/d ln r. The corresponding AOD at 500 nm and the fine mode volume median radius are shown in the legend.

transfer model and (2) derivation from a large ensemble of measurements [*Conant*, 2000; *Li and Trishchenko*, 2001]. Here, a set of empirical equations is first developed to parameterize the surface irradiance as a function of AOD and solar zenith angle. Instantaneous surface irradiances with and without aerosol are then calculated from the parameterization equations and the diurnal ADRF is finally derived through the 24-h integration of instantaneous ADRF.

[17] The SBDART model is run twice using real water vapor in one run and a fixed water vapor in the other run. The ratios of surface irradiance from the two runs are then used to scale the observations to values expected under conditions with the fixed water vapor. The objective is to minimize effects of varying water vapor on the analysis. Figure 7 presents scatterplots of AOD and surface SWR in each of nine solar zenith angle bins. Surface irradiance changes linearly with AOD when AOD is low, but a nonlinear function should be used to describe the overall relationships. Similar relationship between AOD and PAR is also derived (not shown). The following exponential equation is used to fit the data points:

$$F(\theta) = F_0(\theta) \times \exp(b(\theta) \times AOD) \qquad (1)$$

where $F(\theta)$ represents the scaled surface irradiance and $F_0(\theta)$ and $b(\theta)$ are fitting parameters. Measurements and simulations (represented by shaded and solid dots, respectively) are superimposed. $F_0(\theta)$ represents surface irradiance under the background condition, i.e., no aerosol in the

atmosphere. $b(\theta)$ determines the aerosol effect on atmospheric transmission. Figure 8 presents scatterplots of $F_0(\theta)$ and $b(\theta)$ as a function of μ for SWR (Figure 8, top) and PAR (Figure 8, bottom). The data points may be fit by a linear equation [*Chou et al.*, 2006], but a power law equation is used because the former produces incorrect results when θ is 0° or 90°, i.e., $F_0(\theta) = a_1 \times \mu^{a_2}$ and $b(\theta) = a_3 \times \mu^{a_4}$. The four parameters are derived using the least squares technique. Instantaneous global SWR and PAR at the surface can then be parameterized as a function of θ and AOD as follows:

$$F(\theta) = a_1 \times \mu^{a_2} \times \exp[a_3 \times \mu^{a_4} \times AOD] \qquad (2)$$

The instantaneous aerosol direct forcing ($ADRF_{int} = (1 - \alpha) \times (F(\theta) - F_0(\theta))$) can then be computed, where α represents the surface albedo. This is an important parameter in assessing aerosol effects on climate because of its dramatic spatial and temporal variations. A more useful parameter in climate studies is the diurnal mean aerosol direct radiative forcing ($ADRF_{24hr}$). $ADRF_{24hr}$ represents the climatic effects of aerosol and can be calculated as follows:

$$ADRF_{24hr} = (1 - \alpha) \times \int_0^{24} (a_1 \times \mu^{a_2})$$
$$\times (\exp(a_3 \times \mu^{a_4} \times AOD) - 1) dt / 24hr \qquad (3)$$
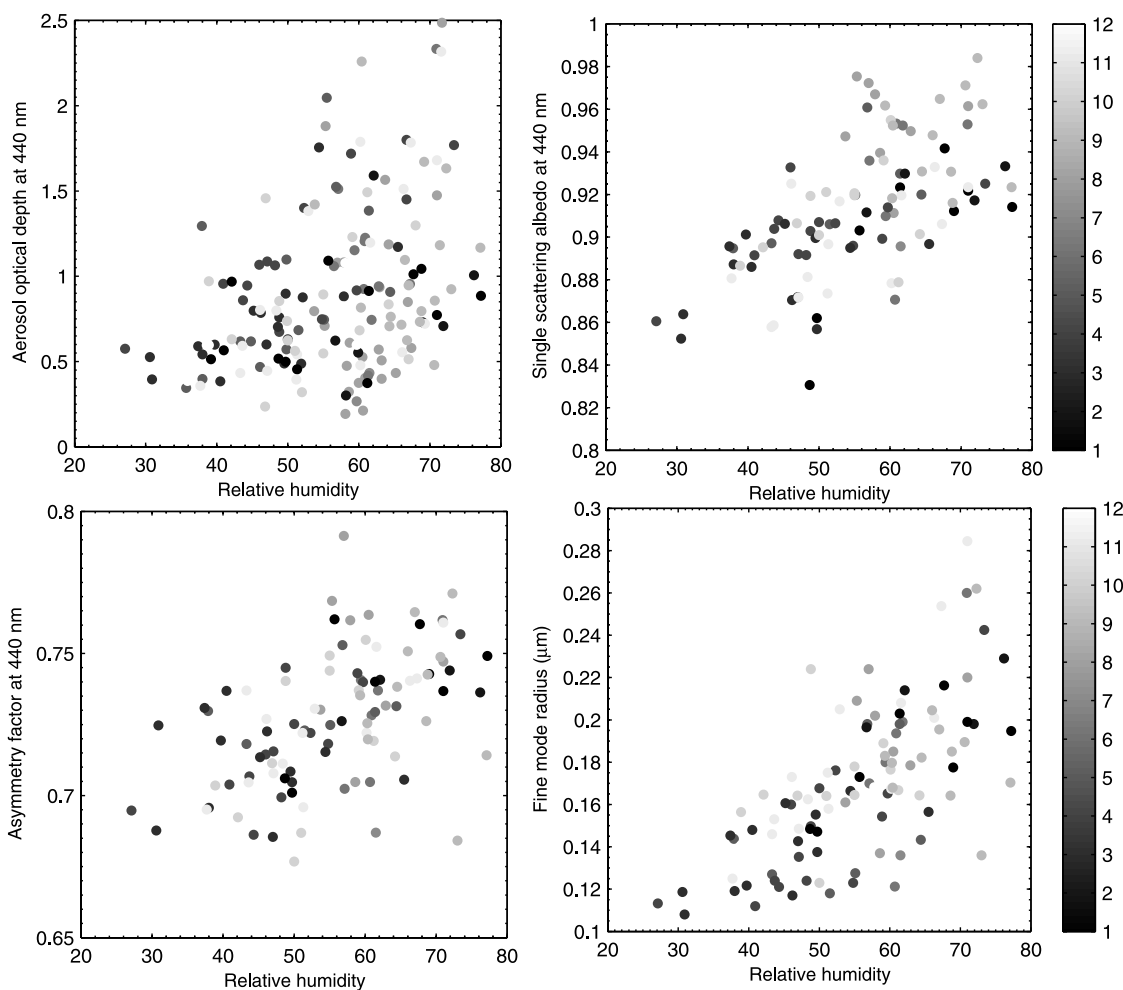
Figure 5. Relationships between relative humidity and the aerosol optical depth, single scattering albedo, asymmetry factor and fine mode radius for data from September 2005 to August 2006. The data points in each month are represented by different shading.

where θ can be computed from latitude and Coordinated Universal Time (UTC) time.

[18] Figure 9 presents monthly mean $ADRF_{24hr}$ for SWR (Figure 9, left) and PAR (Figure 9, right), which are obtained by averaging daily mean $ADRF_{24hr}$. The annual mean $ADRF_{24hr}$ estimated from the measurement and the SBDART is -38.4 W m^{-2} and -39.3 W m^{-2}, respectively. The $ADRF_{24hr}$ here is more than three times that the global average over land (-11.8 ± 1.9W m^{-2}) [Yu et al., 2006]. The annual mean $ADRF_{24hr}$ for PAR from the measurement and the SBDART is -17.8 and -20.1 W m^{-2}, respectively, about half that for SWR. The normalized $ADRF_{24hr}$ ($ADRF_{24hr}$ per unit AOD) here is -51.4 and -23.8 W m^{-2} for SWR and PAR, respectively. Both values are moderately less than those in northern China where the values are -55.2 and -28.0 W m^{-2} [Xia et al., 2007c]. This is accordance with the fact that both SSA and ASY here are larger than those in northern China.

## 4.4. Aerosol Effects on the Partitioning of Direct and Diffuse Radiation

[19] Surface radiation data measured by the pyranometer network in China show that the average amount of surface irradiance has gone down by almost 3.3% per decade during the period of 1960 to 2000 in China. This coincided with drops in cloud cover and rainy day during the same time [Liang and Xia, 2005; Qian et al., 2006]. It is speculated that increased aerosol loading leads to less irradiance reaching the Earth's surface via both the direct and indirect cloud effects. The optimal yields of crops in China are believed to decrease by the same percentage of decline as the surface irradiance [Chameides et al., 1999]. Note however that the benefit of the increase in diffuse SWR due to aerosols for crop growth was not considered in the analysis. As a matter of fact, it is widely recognized that a high proportion of diffuse radiation is able to increase the radiation use efficiency by a canopy and has much less tendency to cause canopy photosynthetic saturation [Gu et al., 2002]. Therefore it is useful to determine how much direct radiation is transformed into diffuse radiation via aerosol scattering and how these changes in the partitioning impact crop yield and carbon cycling.

[20] Scatterplots of measured direct and diffuse SWR as a function of AOD for nine θ ranges are shown in Figures 10 and 11. Relationships between direct, diffuse PAR and AOD are also derived, but from SBDART simulations (not shown). Note that direct radiation decreases significantly because of aerosol scattering and absorption. The presence
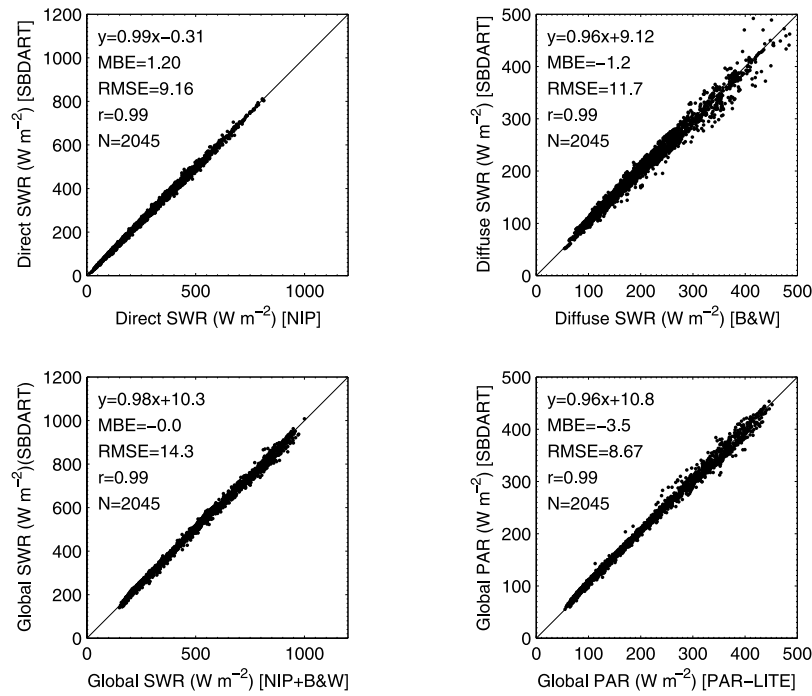
Figure 6. Comparisons between the model simulations and the observations of (top left) direct, (top right) diffuse, (bottom left) global, and (bottom right) PAR radiation (unit is W m^{-2}).
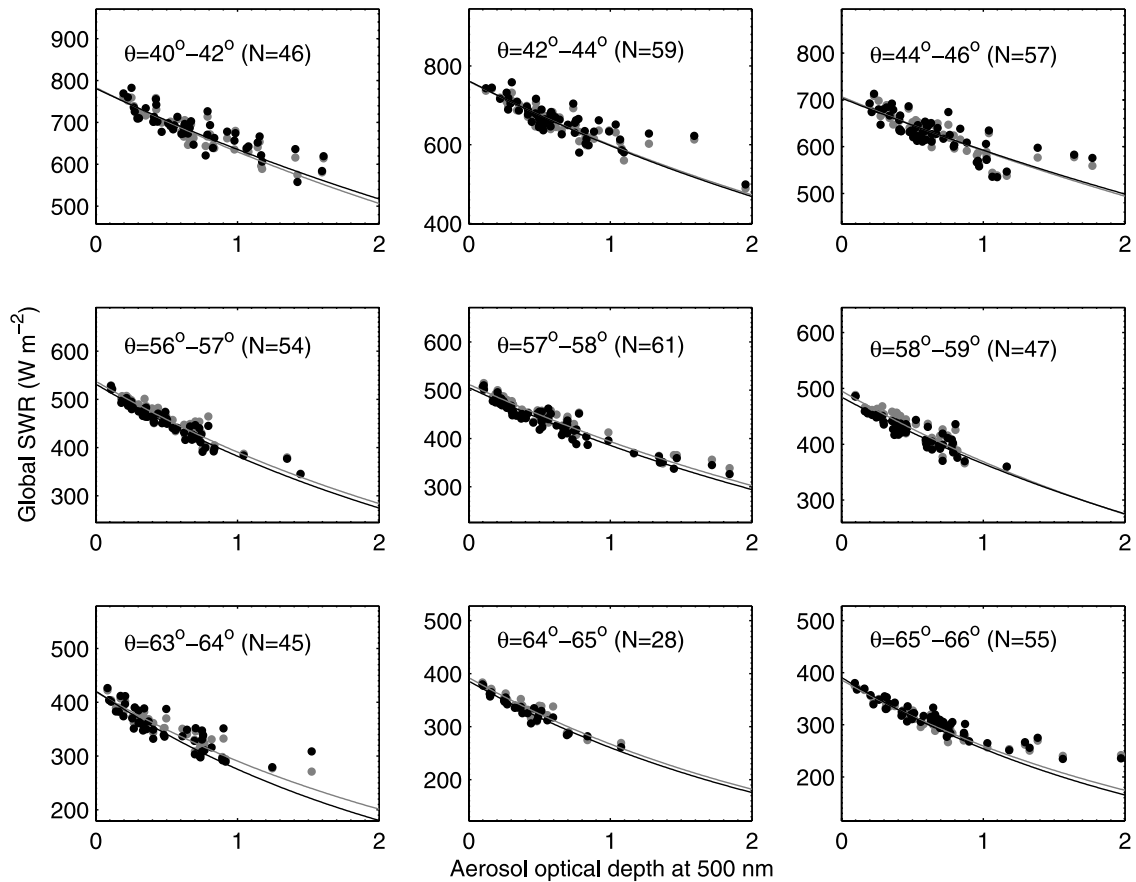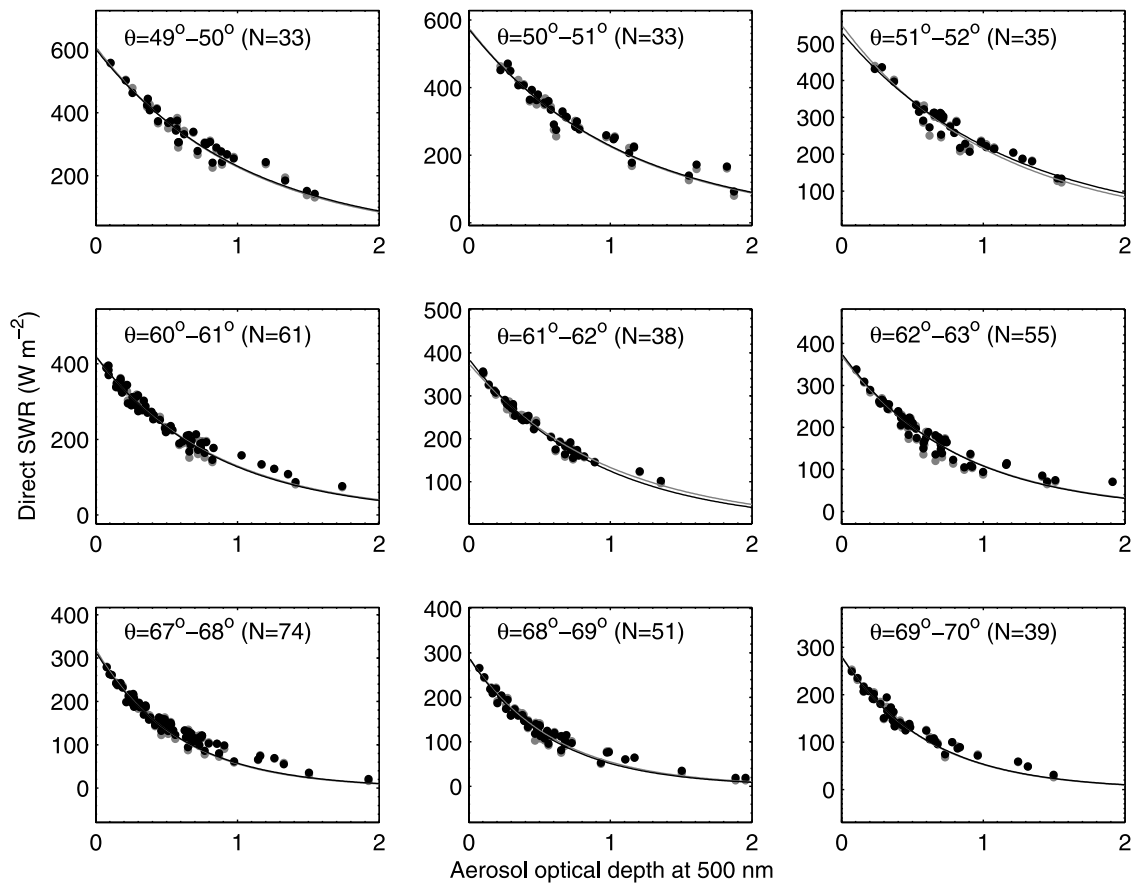

Figure 7. Scatterplots of global shortwave irradiance as a function of the aerosol optical depth at 500 nm for nine solar zenith angles. Measurements and model simulations are represented by shaded and solid dots, respectively. The shaded and solid curves represent the fitting results using an exponential equation to the measurement and model simulation, respectively.
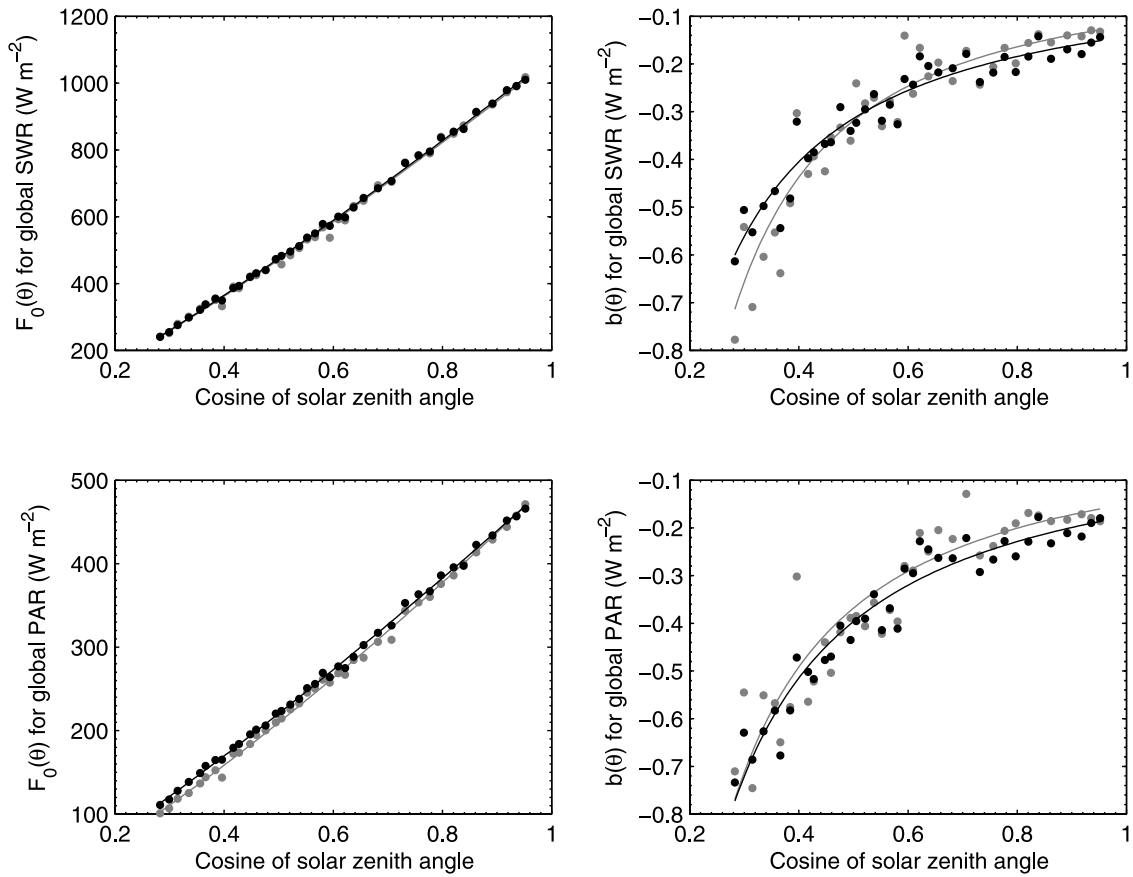
Figure 8. Scatterplots of parameters $F_0(\theta)$ and $b(\theta)$ as a function of the cosine of the solar zenith angle for (top) global shortwave irradiance and (bottom) global PAR.
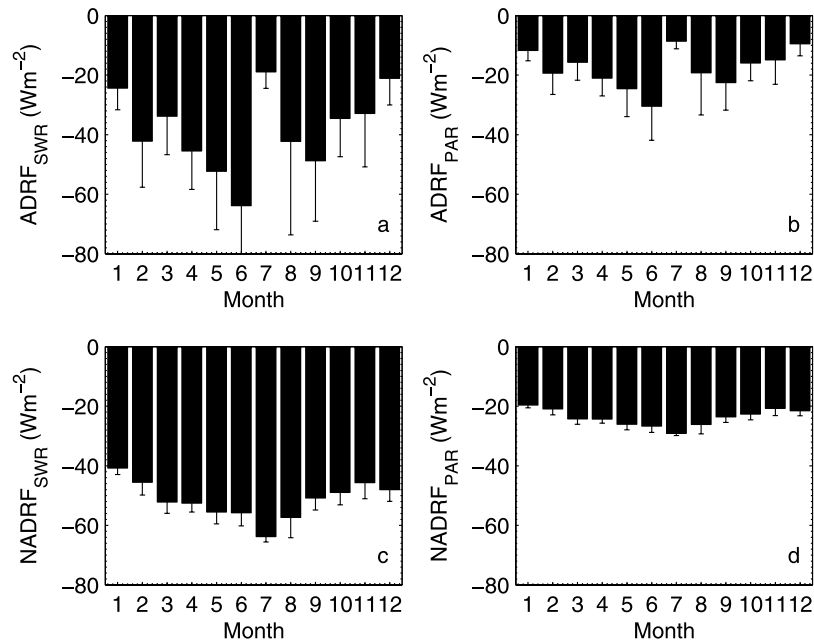
Figure 9. Monthly diurnal mean aerosol direct radiative forcing at the surface (ADRF) and corresponding ADRF per unit AOD (NADRF) (left) for global shortwave radiation and (right) for global photosynthetically active radiation.

**Figure 10.** Same as Figure 7 but for direct shortwave irradiance.
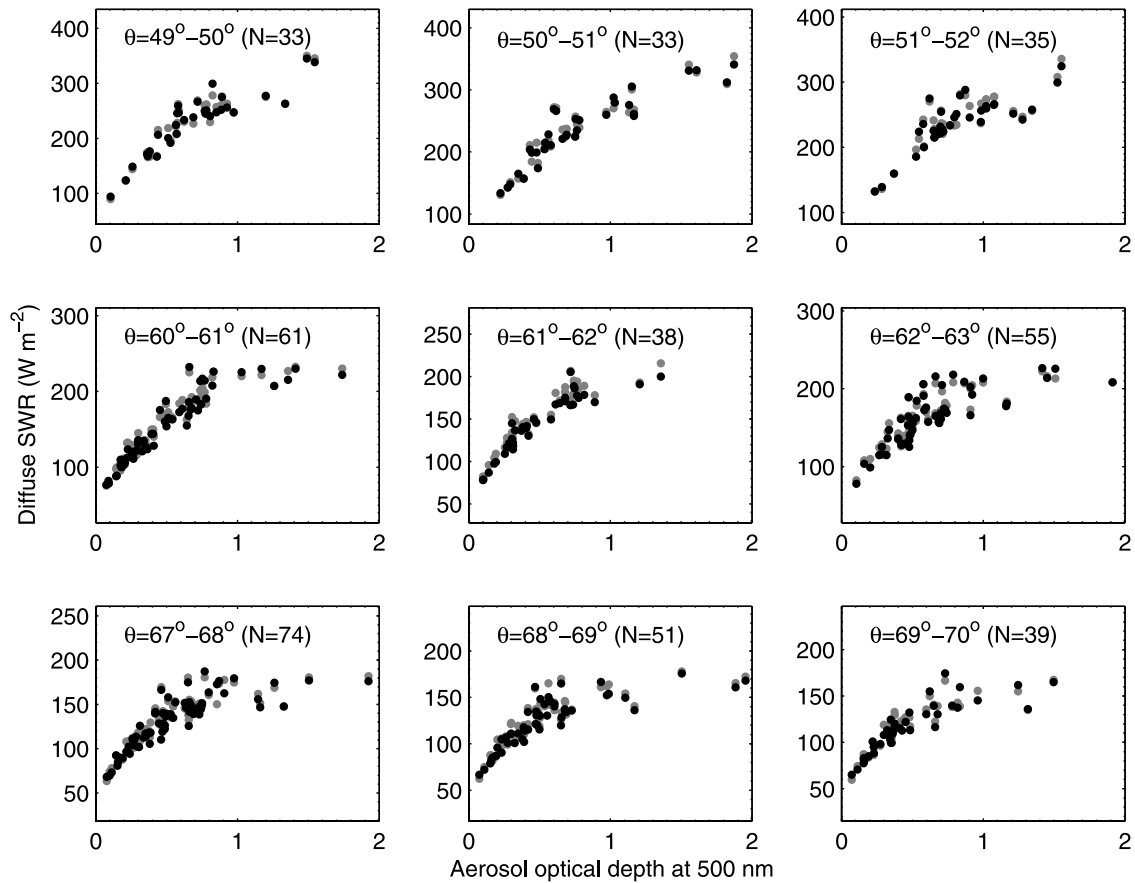
Figure 11. Scatterplots of diffuse shortwave irradiance as a function of the aerosol optical depth at 500 nm for nine solar zenith angles. Measurements and model simulations are represented by shaded and solid dots, respectively.

of heavy aerosol loading significantly enhances the diffuse radiation. Similar analysis is performed regarding the relationship between direct radiation and AOD as that between global radiation and AOD. Therefore monthly changes in surface direct radiation induced by aerosols are calculated, which are then combined with the changes in global irradiance to produce the monthly changes in surface diffuse irradiance. Figure 12 presents the monthly changes in surface global, direct and diffuse radiation induced by aerosols in the SW and PAR spectra, respectively. The
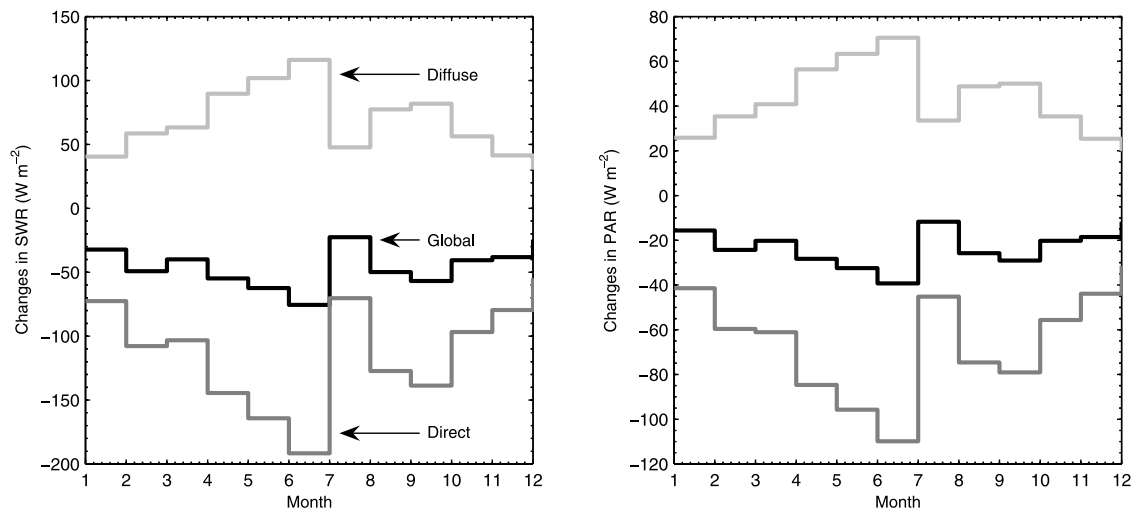
Figure 12. Monthly changes in surface global, direct and diffuse irradiance induced by aerosols for (left) shortwave irradiance and (right) photosynthetically active radiation.
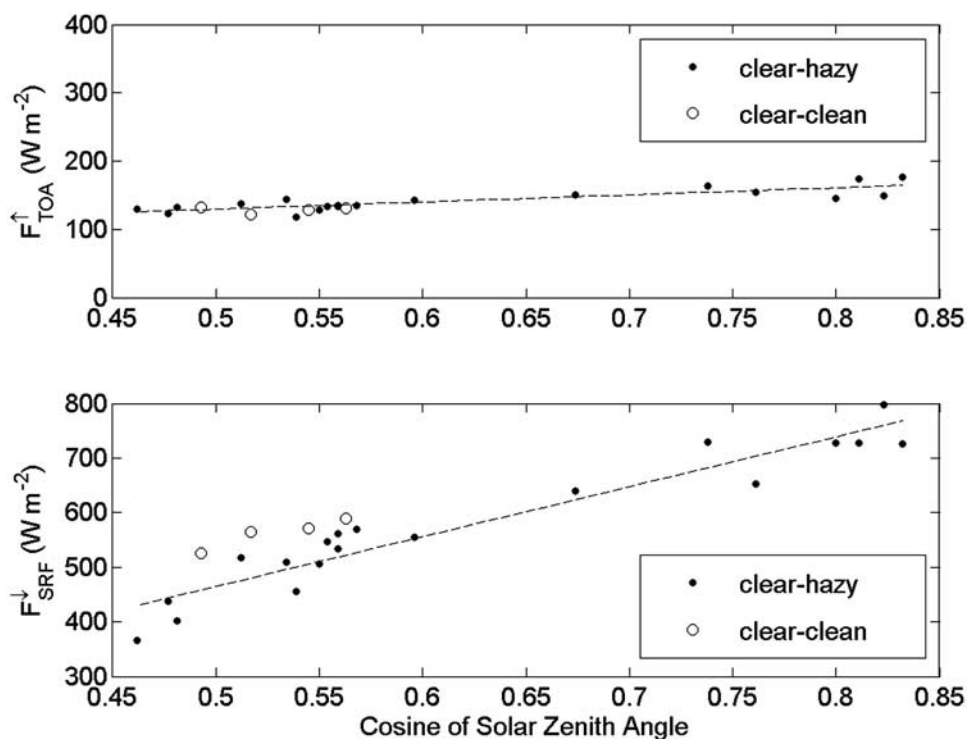
Figure 13. Solar irradiance (top) reflected at the top of the atmosphere from the CERES SSF product and (bottom) incoming on the ground measured on the ground for clear-clean (AOD < 0.2) and clear-hazy conditions (AOD > 0.2) at Taihu. Data are from September to December 2005.

presence of heavy aerosol loading in eastern China induced a significant change in the partitioning of surface irradiance. The annual reduction in direct and global SWR due to aerosol is -112.6 W m^{-2} and -45.5 W m^{-2} and aerosol leads to 67.1 W m^{-2} more diffuse SWR reaching the Earth's surface. With regard to PAR, the annual mean differences in global, direct and diffuse irradiance are -23.1 W m^{-2}, -65.2 W m^{-2} and 42.1 W m^{-2} with and without the presence of aerosol, respectively. Global, direct and diffuse SWR with the presence of aerosol is 82%, 51% and 377% that without aerosol. The ratios are 80%, 40% and +649% for global, direct and diffuse PAR, respectively.

4.5. TOA Aerosol Forcing at Taihu

[21] The CERES satellite data are matched with surface measurements that are classified as being clear-clean and clear-hazy sky conditions. Clear-cloudy classification was done following the procedure as explained above, while clear and hazy conditions are determined by aerosol optical depth (AOD < 0.2 for clean). Separate scatterplots are generated for TOA reflected fluxes and surface downwelling SW fluxes as functions of μ (Figure 13). In contrast to the clear separation between clear and hazy data on the surface plot, there is a no clear distinction for the TOA data points. This implies that the addition of heavy aerosols in the region does not increase instantaneous reflection in the atmosphere-surface system. Changes in TOA reflection are dictated by a combination of aerosol parameters (SSA, AOD, backscattering fraction) and surface albedo. It is a

coincidence that this combination of variables results in a near neutral aerosol effect.

5. Discussion

[22] It is widely recognized that the SSA is a key parameter influencing aerosol forcing and satellite remote sensing of AOD. Note that the aerosol SSA in the MODIS aerosol algorithm was recently lowered from 0.95 to 0.85 in eastern China [*Remer et al.*, 2005; *Mi et al.*, 2007]. Precipitation and temperature changes in a climate model were comparable to those observed if the aerosols contain a large proportion of absorbing black carbon (the SSA equal to 0.85) [*Menon et al.*, 2002]. The substantial difference in the magnitude of the SSA between AERONET retrievals here and those assigned in the satellite aerosol algorithms and the model simulations indicates that much more information is needed about the aerosol absorption in this region.

[23] The diffuse fraction of surface SWR and PAR increased by more than four and eight times because of heavy aerosol in eastern China, respectively. The large change in the partitioning of surface irradiance is a significant atmospheric forcing which needs to be considered in the crop simulation models. Further studies are required to figure out the overall effects of aerosol on crop growth, in which both advantages and disadvantages of haze in China should be thoroughly considered.

6. Conclusions

[24] Solar broadband and spectral radiation were measured by a set of radiometers since September 2005 at the

Taihu site, the second EAST-AIRE supersite. One year's worth of aerosol and radiation data were combined and the parameterization schemes were developed to quantitatively estimate the aerosol radiative effects. Significant aerosol effects on SWR and PAR were revealed in this paper.

[25] The annual mean AOD approaches 0.77 and the annual AWE is 1.17. The AOD at the Taihu site is equal to or moderately larger than the measurements obtained at other urban and suburban regions in China. The SSA at 440 nm is about 0.90, which is larger than that used in the MODIS aerosol algorithm and in some climate model simulations. The SSA and ASY in this region are moderately larger than those in northern China.

[26] Heavy aerosol loading in the atmosphere at the Taihu site leads to a significant reduction in surface global irradiance. The annual mean ADRFs at the surface estimated from the measurements for SWR and PAR is -38.4 W m^{-2} and -17.8 W m^{-2}, respectively. In contrast to the strong negative radiative forcing at the surface, the forcing at the top of the atmosphere is almost nil because of aerosol moderate absorption.

[27] The annual reduction in direct and global SWR due to aerosol is -112.6 W m^{-2} and -45.5 W m^{-2} and aerosol leads to 67.1 W m^{-2} more diffuse SWR reaching the Earth's surface. With regard to PAR, the annual mean differences in global, direct and diffuse irradiance are -23.1 W m^{-2}, -65.2 W m^{-2} and 42.1 W m^{-2} with and without the presence of aerosol, respectively.

References

Chameides, W. L., et al. (1999), Case study of the effects of atmospheric aerosols and regional haze on agriculture: An opportunity to enhance crop yields in China through emission controls?, *Proc. Natl. Acad. Sci. U. S. A.*, 96, 13,626–13,633.

Cheng, T. T., Y. Liu, D. R. Lu, Y. F. Xu, and H. Y. Li (2006), Aerosol properties and radiative forcing in Hunshan Dake desert, northern China, *Atmos. Environ.*, 40, 2169–2179.

Chou, M. D., P. H. Lin, P. L. Ma, and H. J. Lin (2006), Effects of aerosols on the surface solar radiation in a tropical urban area, *J. Geophys. Res.*, 111, D15207, doi:10.1029/2005JD006910.

Conant, W. C. (2000), An observational approach for determining aerosol surface radiative forcing: Results from the first field phase of INDOEX, *J. Geophys. Res.*, 105, 15,347–15,360.

Dubovik, O., et al. (2000), Accuracy assessments of aerosol optical properties retrieved from AERONET Sun and sky radiance measurements, *J. Geophys. Res.*, 105, 9791–9806.

Dubovik, O., B. N. Holben, T. F. Eck, A. Smirnov, Y. J. Kaufman, M. D. King, D. Tanre, and I. Slutsker (2002), Variability of absorption and optical properties of key types observed in worldwide locations, *J. Atmos. Sci.*, 59, 590–608.

Dubovik, O., et al. (2006), Application of spheroid models to account for aerosol particle nonsphericity in remote sensing of desert dust, *J. Geophys. Res.*, 111, D11208, doi:10.1029/2005JD006619.

Dutton, E. G., J. J. Michalsky, T. Stoffel, B. W. Forgan, J. Hickey, D. W. Nelson, T. L. Alberta, and I. Reda (2001), Measurement of broadband diffuse solar irradiance using current commercial instrumentation with a correction for thermal offset errors, *J. Atmos. Oceanic Technol.*, 18(3), 297–314.

Eck, T. F., B. N. Holben, J. S. Reid, O. Dubovik, A. Smirnov, N. T. O'Neill, I. Slutsker, and S. Kinne (1999), Wavelength dependence of the optical depth of biomass burning, urban and desert dust aerosols, *J. Geophys. Res.*, 104, 31,333–31,350.

Eck, T. F., et al. (2005), Columnar aerosol optical properties at AERONET sites in central eastern Asia and aerosol transport to the tropical mid-Pacific, *J. Geophys. Res.*, 110, D06202, doi:10.1029/2004JD005274.

Gu, L., D. Baldocchi, S. B. Verma, T. A. Black, T. Vesala, E. M. Falge, and P. R. Dowty (2002), Advantages of diffuse radiation for terrestrial ecosystem productivity, *J. Geophys. Res.*, 107(D6), 4050, doi:10.1029/2001JD001242.

Halthore, R. N., et al. (2005), Intercomparison of shortwave radiative transfer codes and measurements, *J. Geophys. Res.*, 110, D11206, doi:10.1029/2004JD005293.

Holben, B. N., et al. (1998), AERONET—A federated instrument network and data archive for aerosol characterization, *Remote Sens. Environ.*, 66, 1–16.

Li, X. W., X. J. Zhou, and W. L. Li (1995), The cooling of Sichuan province in recent 40 years and its probable mechanism, *Acta Meteorol. Sinica*, 9, 57–68.

Li, Z. (2004), Aerosol and climate: A perspective from east Asia, in *Observation, Theory, and Modeling of the Atmospheric Variability*, pp. 501–525, World Sci., Hackensack, N. J.

Li, Z., and A. Trishchenko (2001), Quantifying the uncertainties in determining SW cloud radiative forcing and cloud absorption due to variability in atmospheric condition, *J. Atmos. Sci.*, 58, 376–389.

Li, Z., et al. (2007a), Aerosol optical properties and their radiative effects in norhern China, *J. Geophys. Res.*, 112, D22S01, doi:10.1029/2006JD007382.

Li, Z., et al. (2007b), Preface to special section on East Asian Studies of Tropospheric Aerosols: An International Regional Experiment (EAST-AIRE), *J. Geophys. Res.*, doi:10.1029/2007JD008853, in press.

Li, Z., F. Niu, K. H. Lee, J. Xin, W. M. Hao, B. Nordgren, Y. Wang, and P. Wang (2007c), Validation and understanding of Moderate Resolution Imaging Spectroradiometer aerosol products (C5) using ground-based measurements from the handheld Sun photometer network in China, *J. Geophys. Res.*, 112, D22S07, doi:10.1029/2007JD008479.

Liang, F., and X. Xia (2005), Long-term trends in solar radiation and the associated climatic factors over China for 1961–2000, *Ann. Geophys.*, 23, 2425–2432.

Long, C. N., and T. P. Ackerman (2000), Identification of clear skies from broadband pyranometer measurements and calculation of downwelling shortwave cloud effects, *J. Geophys. Res.*, 105, 15,609–15,626.

Luo, Y., D. Lu, X. Zhou, W. Li, and Q. He (2001), Characteristics of the spatial distribution and yearly variation of aerosol optical depth over China in last 30 years, *J. Geophys. Res.*, 106(D13), 14,501–14,514.

Mao, J. T., and C. C. Li (2005), Observation study on aerosol radiative properties over China (in Chinese), *Acta Meteorol. Sinica*, 63, 622–635.

Menon, S., J. E. Hansen, L. Nazarenko, and Y. F. Luo (2002), Climate effects of black carbon aerosols in China and India, *Science*, 297, 2249–2252.

Mi, W., Z. Li, X. Xia, B. Holben, R. Levy, F. Zhao, H. Chen, and M. Cribb (2007), Evaluation of the Moderate Resolution Imaging Spectroradiometer aerosol products at two Aerosol Robotic Network stations in China, *J. Geophys. Res.*, 112, D22S08, doi:10.1029/2007JD008474.

Michalsky, J., E. Dutton, D. Nelson, M. Rubes, T. Stoffel, M. Wesley, M. Splitt, and J. DeLuisi (1999), Optimal measurement of surface shortwave irradiance using current instrumentation, *J. Atmos. Oceanic Technol.*, 16, 55–69.

Ohmura, A., et al. (1998), Baseline Surface Radiation Network (BSRN/WCRP): New precision radiometry for climate research, *Bull. Am. Meteorol. Soc.*, 79, 2115–2136.

Qian, Y., D. P. Kaiser, L. R. Leung, and M. Xu (2006), More frequent cloud-free sky and less surface solar radiation in China from 1955 to 2000, *Geophys. Res. Lett.*, 33, L01812, doi:10.1029/2005GL024586.

Qiu, J. H., and L. Q. Yan (2000), Variation characteristics of atmospheric optical depths and visibility in north China during 1980–1994, *Atmos. Environ.*, 34, 603–609.

Qiu, J. H., L. Q. Yan, and X. Y. Zhang (2004), Characteristics of the imaginary part and single-scattering albedo of urban aerosols in northern China, *Tellus, Ser. B*, 56, 276–284.

Ramanathan, V., P. J. Crutzen, J. T. Kiehl, and D. Rosenfeld (2001), Aerosols, climate, and the hydrological cycle, *Science*, 294, 2119–2124.

Remer, L. A., et al. (2005), The MODIS aerosol algorithm, products and validation, *J. Atmos. Sci.*, 62, 947–973.

Ren, L., R. G. You, W. X. Lu, W. Zhang, and X. L. Wang (1999), The physical and chemical characteristics of aerosols in the urban region and their influence on human health (in Chinese), *Clim. Environ. Res.*, 4, 67–73.

Ricchiazzi, P., S. Yang, C. Gautier, and D. Sowle (1998), SBDART: A research and teaching software tool for plane-parallel radiative transfer in the Earth's atmosphere, *Bull. Am. Meteorol. Soc.*, 79, 2101–2114.

Schaaf, C. B., et al. (2002), First operational BRDF, albedo and nadir reflectance products from MODIS, *Remote Sens. Environ.*, 83, 135–148.

Song, L., and D. Lu (2006), Observation of atmospheric aerosol optical properties over Shanghai area (in Chinese), *Clim. Environ. Res.*, *2*, 203–208.

Stoffel, T. (2005), Solar Infrared Radiation Station handbook, *ARM Tech. Rep. ARM-TR-035,* Natl. Renewable Energy Lab., Golden, Colo. (Available at http://www.arm.gov)

Wang, M. (1999), *Atmospheric Chemistry* (in Chinese), Chin. Meteorol. Press, Beijing.

Wang, M., R. Zhang, and Y. Pu (2001), Recent researches on aerosol in China, *Adv. Atmos. Sci.*, *18*, 576–586.

Wielicki, B. A., et al. (1996), Clouds and the Earth's Radiative Energy System (CERES): An Earth observing system experiment, *Bull. Am. Meteorol. Soc.*, *76*, 2125–2153.

Xia, X., H. Chen, P. Wang, X. Zong, P. Gouloub, and J. Qiu (2005), Aerosol properties and their spatial and temporal variations over north China in spring 2001, *Tellus, Ser. B*, *57*, 28–39.

Xia, X., et al. (2006), Variation of column-integrated aerosol properties in a Chinese urban region, *J. Geophys. Res.*, *111*, D05204, doi:10.1029/2005JD006203.

Xia, X., H. Chen, P. Goloub, W. Zhang, B. Chatenet, and P. Wang (2007a), A complication of aerosol optical properties and calculation of direct radiative forcing over an urban region in northern China, *J. Geophys. Res.*, *112*, D12203, doi:10.1029/2006JD008119.

Xia, X., Z. Li, P. Wang, H. Chen, and M. Cribb (2007b), Estimation of aerosol effects on surface irradiance based on measurements and radiative transfer model simulations in northern China, *J. Geophys. Res.*, *112*, D22S10, doi:10.1029/2006JD008337.

Xia, X., H. Chen, Z. Li, P. Wang, and J. Wang (2007c), Significant reduction of surface solar irradiance induced by aerosols in a suburban region in northeastern China, *J. Geophys. Res.*, *112*, D22S02, doi:10.1029/2006JD007562.

Xu, J., M. H. Bergin, X. Yu, G. Liu, J. Zhao, C. M. Carrico, and K. Baumann (2002), Measurement of aerosol chemical, physical and radiative properties in the Yangtze delta region of China, *Atmos. Environ.*, *36*, 161–173.

Xu, J., M. H. Bergin, R. Greenwald, and P. B. Russell (2003), Direct aerosol radiative forcing in the Yangtze delta region of China: Observation and model estimation, *J. Geophys. Res.*, *108*(D2), 4060, doi:10.1029/2002JD002550.

Xu, Q. (2001), Abrupt change of the midsummer climate in central east China by the influence of atmospheric pollution, *Atmos. Environ.*, *35*, 5029–5040.

Yu, H., et al. (2006), A review of measurement-based assessments of the aerosol direct radiative effect and forcing, *Atmos. Chem. Phys.*, *6*, 613–666.

Zhang, J. H., J. T. Mao, and M. H. Wang (2002), Analysis of aerosol extinction characteristics in different area of China, *Adv. Atmos. Sci.*, *19*, 136–152.

Zong, X. M., J. H. Qiu, and P. C. Wang (2005), Characteristics of atmospheric aerosol optical depth over 16 radiation stations in the last 10 years (in Chinese), *Clim. Environ. Res.*, *10*, 201–208.

————————————

H. Chen, P. Wang, and X. Xia, Laboratory for Middle Atmosphere and Global Environment Observation, Institute of Atmospheric Physics, Chinese Academy of Sciences, Beijing 100021, China. (xiaxiangao2000@yahoo.com)

M. Cribb and Z. Li, Department of Atmospheric and Oceanic Science, University of Maryland, College Park, MD 20742, USA.

T. Eck and B. Holben, Laboratory for Atmospheres, Code 613, NASA Goddard Space Flight Center, Greenbelt, MD 20771, USA.

Y. Zhao, Chinese Academy of Meteorological Sciences, Chinese Meteorological Administration, Beijing 100089, China.